



# Interfacial engineering enables surface lattice oxygen activation of SmMn<sub>2</sub>O<sub>5</sub> for catalytic propane combustion



Yi Liu <sup>a</sup>, Haolu Hu <sup>a</sup>, Jiamin Zheng <sup>a</sup>, Fei Xie <sup>a</sup>, Huayu Gu <sup>a</sup>, Sadegh Rostamnia <sup>c,\*</sup>, Fangfang Pan <sup>a,\*</sup>, Xiao Liu <sup>a,\*</sup>, Lizhi Zhang <sup>a,b</sup>

<sup>a</sup> Key Laboratory of Pesticide & Chemical Biology of Ministry of Education, College of Chemistry, Central China Normal University, Wuhan 430079, PR China

<sup>b</sup> School of Environmental Science and Engineering, Shanghai Jiao Tong University, Shanghai 200240, PR China

<sup>c</sup> Organic and Nano Group, Department of Chemistry, Iran University of Science and Technology, Tehran 16846-13114, Iran

## ARTICLE INFO

### Keywords:

Mullite SmMn<sub>2</sub>O<sub>5</sub>  
Lattice oxygen activation  
Propane oxidation  
Interface regulation  
Electron transfer

## ABSTRACT

Surface lattice oxygen ( $O_{latt}$ ) over transition metal oxides plays a pivotal role in catalytic combustion of automobile exhaust. The insufficient  $O_{latt}$  activity at low temperatures, however, remains the key problem restricting its practical application. To overcome this deficiency, we activated the  $O_{latt}$  of mullite SmMn<sub>2</sub>O<sub>5</sub> through the interface fabrication with spinel Co<sub>3</sub>O<sub>4</sub>. The optimized Co<sub>3</sub>O<sub>4</sub>/SmMn<sub>2</sub>O<sub>5</sub> catalyst exhibited 90% conversion at 247 °C for the typical automobile exhaust propane combustion, 77 °C lower than the original SmMn<sub>2</sub>O<sub>5</sub>. Additionally, Co<sub>3</sub>O<sub>4</sub>/SmMn<sub>2</sub>O<sub>5</sub> showed extremely high stability even under harsh operating temperature (e.g., 800 °C). Experimental and theoretical calculation results revealed that the regulated interface of Co<sub>3</sub>O<sub>4</sub>/SmMn<sub>2</sub>O<sub>5</sub> facilitated the electrons transfer from SmMn<sub>2</sub>O<sub>5</sub> to Co<sub>3</sub>O<sub>4</sub>, contributing to the enhanced propane adsorption and catalytic oxidation activity due to the formation of electrophilic oxygen in SmMn<sub>2</sub>O<sub>5</sub> around the interface. This work can provide a basic understanding of the  $O_{latt}$  activation for developing efficient automobile exhaust combustion catalysts.

## 1. Introduction

Along with the increasing attention to atmospheric pollution, environmental regulations such as the emission standards of hydrocarbons in automobile exhaust are continuously upgraded. Catalytic combustion has been widely used in the treatment of various hydrocarbons due to its ability to efficiently convert hydrocarbons into non-toxic water and carbon dioxide at lower temperatures [1–3]. Nevertheless, the catalytic hydrocarbon combustion currently faces two main challenges: (i) the large emission of hydrocarbons during the cold start of automobiles requires the high low-temperature catalytic oxidation performance of the catalysts; (ii) the high thermal stability of catalysts is also demanded on account of the instantaneously high temperature (> 800 °C) during the operation of the automobile [4–6]. Given that the commonly supported noble metals are high-cost and easy to be deactivated at high temperatures [7–9], mullite-type manganese-based catalysts are regarded as one of the most promising catalysts for hydrocarbons oxidation because of their characteristics of various valences, simple preparation method, high thermal stability, and large reserves [10–12]. Mullite-type

SmMn<sub>2</sub>O<sub>5</sub>, as one of the common manganese-based catalysts, has been studied for selective catalytic NO<sub>x</sub> reduction and volatile organic compounds (VOCs) combustion [13–15]. However, the low-temperature combustion activity of SmMn<sub>2</sub>O<sub>5</sub> is not gratifying due to the inactive  $O_{latt}$ , which is found to be responsible for the combustion reactions [16]. Hence, exploring an efficient and low-cost way to activate the  $O_{latt}$  of SmMn<sub>2</sub>O<sub>5</sub> at low temperatures is of vital importance.

The modulation of charge density is indispensable for the  $O_{latt}$  activation on SmMn<sub>2</sub>O<sub>5</sub>, which can be effectively achieved by interfacial engineering [17,18]. Simultaneously, electron-deficient active oxygen O<sup>2-x</sup>, also called electrophilic oxygen, is capable of facilitating the adsorption and subsequent oxidation of hydrocarbon molecules [17]. Therefore, constructing the interface with the aid of a suitable metal oxide on SmMn<sub>2</sub>O<sub>5</sub> to lower  $O_{latt}$  charge density and thus activate it attracts our attention. Here, the electron transfer direction at the interface is crucial and might be predicted by work function (WF), defined as the minimum energy necessary to drive electrons movement from the solid interior to the surface [19,20]. The interface electrons would migrate between the different phases against the WF gradient

\* Corresponding authors.

E-mail addresses: [rostamnia@iust.ac.ir](mailto:rostamnia@iust.ac.ir) (S. Rostamnia), [ffpan@ccnu.edu.cn](mailto:ffpan@ccnu.edu.cn) (F. Pan), [liuxiao71@ccnu.edu.cn](mailto:liuxiao71@ccnu.edu.cn) (X. Liu).

until the Fermi energy levels of the two phases at the interface reach equilibrium. Accordingly, interfacing mullite with materials possessing larger WF values may hold promise to convert mullite  $O_{latt}$  from inactive  $O^{2-}$  to active  $O^{2-x}$  [18], attributed to electron transfer from mullite to the latter. Among the conventional metal oxides,  $Co_3O_4$  is featured with low cost, wide source, good stability, and large WF value [21], which has the potential advantage of being used to construct the heterogeneous interface with  $SmMn_2O_5$  to activate the  $O_{latt}$ .

Herein, we modified the  $SmMn_2O_5$  surface with  $Co_3O_4$  through an *in situ* growth method. HRTEM showed that the grown  $Co_3O_4$  nanoparticles with the size of 5–10 nm were attached on the surface of the parent  $SmMn_2O_5$ . The results of XPS,  $H_2$ -TPR,  $O_2$ -TPD and DFT calculation revealed the successful activation of the  $O_{latt}$  around the interface of  $Co_3O_4/SmMn_2O_5$  catalyst, rooting in the strong interactions at the interface that facilitated the electron transfer from the  $O$  sites of  $SmMn_2O_5$  to  $Co_3O_4$ . Consequently, the optimized  $Co_3O_4/SmMn_2O_5$  exhibited much enhanced catalytic activity in typical automobile exhaust propane combustion compared with the pure  $Co_3O_4$  and  $SmMn_2O_5$ .

## 2. Experimental section

### 2.1. Chemicals and materials

The commercial manganese oxalate tetrahydrate ( $Mn(CH_3COO)_2 \cdot 4H_2O$ ), cobaltous nitrate hexahydrate ( $Co(NO_3)_2 \cdot 6H_2O$ ), hydrogen peroxide ( $H_2O_2$ ) (30 wt%), sodium carbonate ( $Na_2CO_3$ ), and octanol ( $C_8H_{18}O$ ) were obtained from Sinopharm Chemical Reagent. Poly(ethylene glycol)-block-poly(propylene glycol)-block-poly(ethylene glycol) (P127), samarium nitrate hexahydrate ( $Sm(NO_3)_2 \cdot 6H_2O$ ), and tetramethyl ammonium hydroxide ( $C_4H_{13}NO$ ) were purchased from Aladdin, Shanghai, China. All analytical grade chemicals and materials were purchased from commercial suppliers and used without further purification.

### 2.2. Synthesis of $SmMn_2O_5$

The pure phase  $SmMn_2O_5$  was prepared by the co-precipitation method. First, 0.008 mol (3.5558 g) of  $Sm(NO_3)_3 \cdot 6H_2O$  and 0.016 mol (3.9214 g) of  $Mn(CH_3COO)_2 \cdot 4H_2O$  were dissolved in 100 mL of deionized water. Then 0.04 g of F127 surfactant was added to the above solution followed by stirring for 10 min. Afterwards, tetramethyl ammonium hydroxide was added dropwise to adjust the pH to 9. 2 mL of  $H_2O_2$  (30 wt%) was then added and 2 mL of octanol was dropped as defoamer. Tetramethyl ammonium hydroxide was dripped again until the solution pH reached 11. After 2 h of aging with stirring at room temperature, the precipitate filtered out was placed in an oven at 105 °C overnight. Finally, the obtained precursor was put into muffle furnace and kept at 500 and 800 °C successively for 8 h to obtain pure phase  $SmMn_2O_5$ .

### 2.3. Synthesis of $Co_3O_4/SmMn_2O_5$

The composites  $xCo_3O_4/SmMn_2O_5$  with different  $Co_3O_4$  contents were prepared by an *in situ* growth method. First, 0.50 g of pure phase  $SmMn_2O_5$  was dispersed to 50 mL of deionized water with stirring at room temperature for 15 min, and then the suspension was subjected to ultrasonic dispersion treatment for 1 h. After that, a certain amount of  $Co(NO_3)_2 \cdot 6H_2O$  was dissolved in 10 mL of deionized water and added dropwise to the above suspension to ensure that the mass ratio of  $Co_3O_4$  to  $SmMn_2O_5$  is 1%, 5%, 10%, 30% or 50%. Subsequently, 0.50 mol• $L^{-1}$   $Na_2CO_3$  aqueous solution was added to the suspension to adjust the pH to 10. The solution was stirred at room temperature for 2 h, and the precipitate was obtained by centrifugation. Following this, the precursor was washed three times with deionized water and ethanol, and dried in air at 80 °C for 4 h. After cooling down, the precipitate was calcined in

air at 400 °C for 4 h to obtain  $xCo_3O_4/SmMn_2O_5$ , where  $x$  represents the initial mass ratio of  $Co_3O_4$ . Notably,  $Co_3O_4/SmMn_2O_5$  catalyst generally refers to  $30Co_3O_4/SmMn_2O_5$ , unless otherwise stated. The preparation of the monolithic catalyst (labeled as mono  $Co_3O_4/SmMn_2O_5$ ) based on  $30Co_3O_4/SmMn_2O_5$  was described in the [Supplementary Information](#). Furthermore, the pure phase  $Co_3O_4$  reference sample was also prepared using the same deposition and precipitation process as  $xCo_3O_4/SmMn_2O_5$ , except no adding of  $SmMn_2O_5$ . The  $Co_3O_4+SmMn_2O_5$  was obtained by mechanically mixing pure phase  $Co_3O_4$  and  $SmMn_2O_5$  according to actual ratio of  $Co_3O_4$  and  $SmMn_2O_5$  in  $30Co_3O_4/SmMn_2O_5$ .

### 2.4. Activity measurement

Propane oxidation performance was measured in a home-made fixed-bed quartz reactor (internal diameter is 6.0 mm). The inlet and outlet gas compositions were detected by an on-line gas chromatograph (GC, FULI INSTRUMENTS GC9790Plus, China) with a flame ionization detector (FID), a Ni catalyst converter used for converting  $CO_2$  quantitatively into methane and an RB-WAX conventional capillary column (30 m \* 0.32 mm\*0.3  $\mu$ m). The gas mixture consisted of 0.2% propane, 2% oxygen, 5% water and balance gas nitrogen with a weight hourly space velocity (WHSV) of 30,000 mL•g<sup>-1</sup>•h<sup>-1</sup>. The water vapor content was controlled by quantitatively injecting water into the gasification chamber (Suzhou friends experimental equipment Co., FD-PG) and mixing it with the reaction gas by a precision syringe pump (Easy Pump, SPLab01), and the temperature of the gasification chamber was set at 150 °C.

### 2.5. Materials characterizations

The crystal properties of the catalysts were determined by powder X-ray diffraction (XRD, Bruker D8 Advance diffractometer, Germany) and Raman spectroscopy (Thermo Fisher spectrometer, U.S.). Specific surface area and pore structure were analyzed by physisorption (ASAP 2460, U.S.). The Brunauer-Emmett-Teller (BET) specific surface areas were calculated using adsorption data at the relative pressure range of  $P/P_0 = 0.01$ –1. Pore size distributions were calculated from adsorption branch using the Barrett-Joyner-Halenda (BJH) method. Bulk elemental compositions were determined by inductively coupled plasma-atomic emission spectroscopy (ICP-AES, Agilent 725, U.S.). The texture and surface morphology of the catalysts were obtained using a transmission electron microscope (TEM, Tecnai G2 F20 S-TWIN, U.S.) and high-resolution transmission electron microscopy (HR-TEM, Tecnai G2 F20 S-TWIN, U.S.). X-ray photoelectron spectroscopy (XPS) images of the catalysts were recorded on a Thermo ESCALAB 250XI system (U.S.).  $H_2$  temperature-programmed reduction ( $H_2$ -TPR),  $O_2$  temperature-programmed desorption ( $O_2$ -TPD) and  $H_2$  pulse chemisorption were conducted using Autochem II 2920 (U.S.). The signals of  $C_3H_8$  temperature-programmed surface reaction ( $C_3H_8$ -TPSR) and  $C_3H_8$  temperature-programmed desorption ( $C_3H_8$ -TPD) were detected with a mass spectrometer (MS, HRP-20 EGA, U.K.). Density functional theory (DFT) calculations were carried out utilizing the CASTEP and the ultrasoft method. *In situ* diffuse reflectance infrared Fourier transform spectra (DRIFTS) were recorded by Nicolet iS50 spectrometer (Thermo, USA). The details were described in [Supplementary Information](#).

## 3. Results and discussion

### 3.1. Catalytic performance for propane combustion

The catalytic performances of the as-prepared catalysts for propane combustion are shown in [Fig. S1](#). Both  $Co_3O_4$  and  $SmMn_2O_5$  exhibited relatively poor catalytic activity for propane combustion with  $T_{90}$  (reaction temperature when the conversion reached 90%) at 418 and 324 °C, respectively. After loading  $Co_3O_4$  on  $SmMn_2O_5$ , the catalytic performances of the composite  $Co_3O_4/SmMn_2O_5$  were dramatically

improved. The best catalytic activity was achieved when the initial mass ratio of  $\text{Co}_3\text{O}_4$  to  $\text{SmMn}_2\text{O}_5$  was 30%, with  $T_{90}$  of approximately 247 °C, which was 77 and 172 °C lower than that of the pure  $\text{SmMn}_2\text{O}_5$  and  $\text{Co}_3\text{O}_4$ , respectively, and also significantly lower than those of most traditional manganese-based and cobalt-based catalysts listed in Table S1. As the WHSV was elevated to 120,000  $\text{mL}\cdot\text{g}^{-1}\cdot\text{h}^{-1}$ , the  $T_{90}$  of  $\text{Co}_3\text{O}_4/\text{SmMn}_2\text{O}_5$  decreased to 272 °C (Fig. S2), but was still better than most of the reported catalysts. Meanwhile, the comparison of catalytic activity in the presence and absence of water vapor showed that the water resistance of  $\text{Co}_3\text{O}_4/\text{SmMn}_2\text{O}_5$  was significantly superior to that of  $\text{SmMn}_2\text{O}_5$  (Fig. S3). Additionally, to verify the prospect of industrial application of the optimal catalyst, the powder  $\text{Co}_3\text{O}_4/\text{SmMn}_2\text{O}_5$  was coated on cordierite to prepare a monolithic catalyst (Fig. 1a). The  $T_{90}$  of mono  $\text{Co}_3\text{O}_4/\text{SmMn}_2\text{O}_5$  (Fig. 1b) exhibited only a 34 degree drop compared to powder  $\text{Co}_3\text{O}_4/\text{SmMn}_2\text{O}_5$ , showing good scalability. Moreover,  $\text{Co}_3\text{O}_4/\text{SmMn}_2\text{O}_5$  exhibited overwhelmingly high  $\text{CO}_2$  selectivity, which was maintained above 99% after temperatures above 250 °C (Fig. 1c). Additionally, the catalytic rate of  $\text{Co}_3\text{O}_4/\text{SmMn}_2\text{O}_5$  was remarkably superior relative to pure  $\text{SmMn}_2\text{O}_5$  and  $\text{Co}_3\text{O}_4$ , as shown in Fig. 1d. At 150 °C, the catalytic rate of  $\text{Co}_3\text{O}_4/\text{SmMn}_2\text{O}_5$  was several times higher than that of the  $\text{SmMn}_2\text{O}_5$  (39.6 vs. 14.4  $\mu\text{mol}_{\text{propane}}\cdot\text{m}_{\text{cat}}^{-2}\cdot\text{h}^{-1}$ ). From the Arrhenius plots (inset of Fig. 1d), the apparent activation energy of  $\text{Co}_3\text{O}_4/\text{SmMn}_2\text{O}_5$  was only 34.1  $\text{kJ}\cdot\text{mol}^{-1}$ , much lower than those of pure  $\text{SmMn}_2\text{O}_5$  and  $\text{Co}_3\text{O}_4$  (46.7 and 54.5  $\text{kJ}\cdot\text{mol}^{-1}$ , respectively, listed in Table S2). Next, the turnover frequency (TOF) values per surface Mn and Co associated with the propane combustion were determined by using the experimental data obtained at 150 °C (Fig. 1e).  $\text{Co}_3\text{O}_4/\text{SmMn}_2\text{O}_5$  exhibited the highest TOF value with 0.329  $\text{h}^{-1}$ , 2 and 54 times higher than  $\text{SmMn}_2\text{O}_5$  (0.094  $\text{h}^{-1}$ ) and  $\text{Co}_3\text{O}_4$  (0.006  $\text{h}^{-1}$ ), respectively.

The thermal stability of  $\text{Co}_3\text{O}_4/\text{SmMn}_2\text{O}_5$  and mono  $\text{Co}_3\text{O}_4/\text{SmMn}_2\text{O}_5$  for propane combustion was also evaluated. As shown in Fig. 1f, no apparent decline of the propane conversion was detected within 24 h at  $T_{90}$  (247 °C and 280 °C, respectively). Since the practical

temperature of automobile exhaust gas can reach above 800 °C, at which most catalysts were prone to suffering structural collapse thus losing activity, the performance of  $\text{Co}_3\text{O}_4/\text{SmMn}_2\text{O}_5$  and mono  $\text{Co}_3\text{O}_4/\text{SmMn}_2\text{O}_5$  was examined at 800 °C. Clearly, no obvious inactivation occurred, while the crystal structure of the catalyst remained unchanged (Fig. S4). The high activity, superior stability, and remarkable mechanical stability (Fig. S5) suggested the huge potential market of mono  $\text{Co}_3\text{O}_4/\text{SmMn}_2\text{O}_5$  for practical application. Moreover,  $\text{Co}_3\text{O}_4/\text{SmMn}_2\text{O}_5$  exhibited similar catalytic activity within five reaction cycles, indicating the excellent reuse performance for propane combustion (Fig. S6).

### 3.2. Textural and structural characterization

To study the possible influences of catalyst on propane combustion activity, the structure of the composite  $\text{Co}_3\text{O}_4/\text{SmMn}_2\text{O}_5$  was first investigated systematically by various characterization techniques. As represented in Figs. 2a and S7, total characteristic diffraction peaks of XRD patterns belonging to the  $\text{SmMn}_2\text{O}_5$  (PDF 00-052-1096) were observed over all the as-synthesized catalysts except  $\text{Co}_3\text{O}_4$  [11]. The additional weak diffraction peak at 20 of 36.9°, corresponding to the  $\text{Co}_3\text{O}_4$  (PDF 01-078-1969) [22], was only observed when the mass ratio of  $\text{Co}_3\text{O}_4$  to  $\text{SmMn}_2\text{O}_5$  exceeded 30%. The average crystallite size of nanocrystals was estimated by Debye-Scherrer formula and found to be 7.2 nm for  $\text{Co}_3\text{O}_4$  particles over  $\text{SmMn}_2\text{O}_5$  at the mass ratio of 30%, which was similar to the result of TEM. Raman spectra (Fig. 2b) of the two individual catalysts clearly showed all characteristic peaks ascribed to  $\text{SmMn}_2\text{O}_5$  (210, 605 and 677  $\text{cm}^{-1}$ ) and  $\text{Co}_3\text{O}_4$  (196, 481, 520, 621 and 689  $\text{cm}^{-1}$ ) phases [23,24]. After loading  $\text{Co}_3\text{O}_4$  on  $\text{SmMn}_2\text{O}_5$ , a list of new peaks appeared, which were located close to the two individual catalysts, probably due to geometric changes in the  $\text{MnO}$  and  $\text{CoO}$  polyhedra caused by interface interactions in  $\text{Co}_3\text{O}_4/\text{SmMn}_2\text{O}_5$  composite [19,25]. The specific surface area of  $x\text{Co}_3\text{O}_4/\text{SmMn}_2\text{O}_5$  exhibited an increasing tendency with the increase of  $\text{Co}_3\text{O}_4$  loading amount, while the pore size showed an opposite character (Fig. S8 and Table S3).

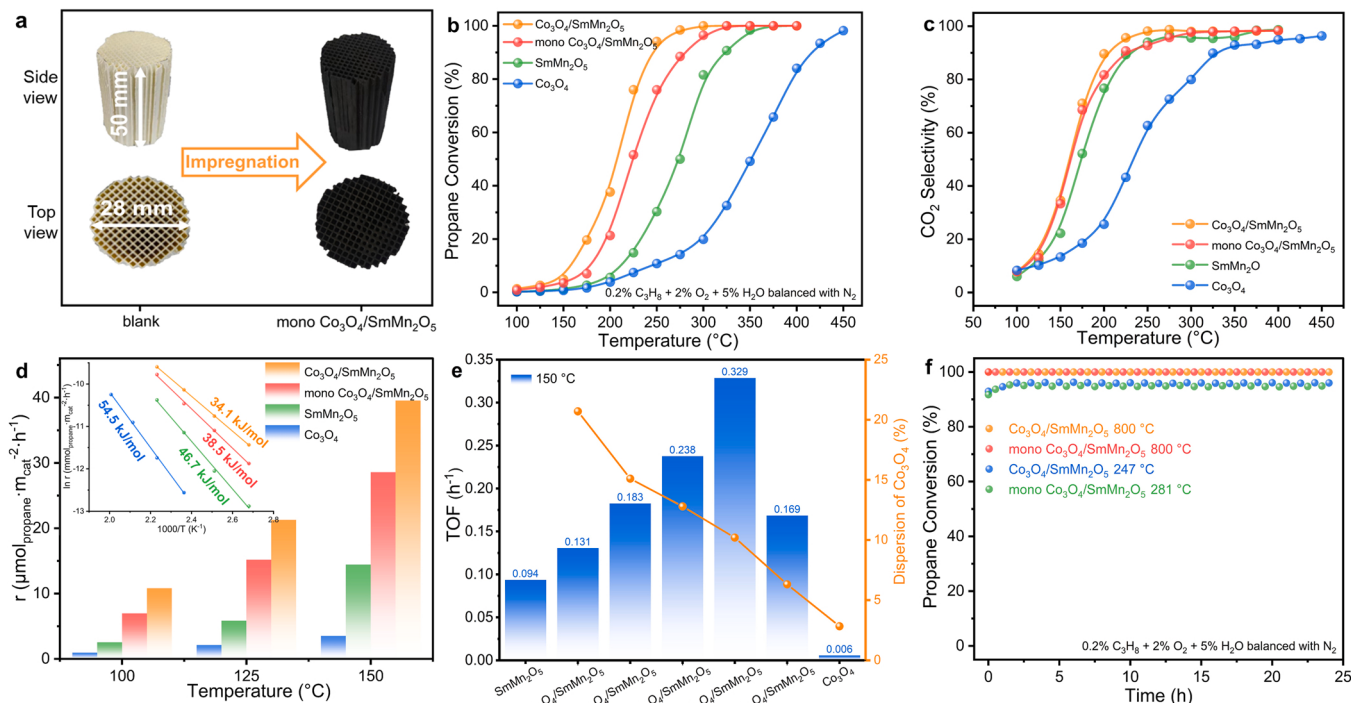


**Fig. 1.** (a) Photographs of cordierite before and after impregnation with  $\text{Co}_3\text{O}_4/\text{SmMn}_2\text{O}_5$ ; (b) propane conversion as a function of temperature over as-prepared catalysts; (c)  $\text{CO}_2$  selectivity as a function of temperature over as-prepared catalysts; (d) reaction rates of propane oxidation (inset: Arrhenius plots and activation energy); (e) TOF of as-prepared catalysts at 150 °C and the dispersion of  $\text{Co}_3\text{O}_4$  particles; (f) catalytic oxidation stability of  $\text{Co}_3\text{O}_4/\text{SmMn}_2\text{O}_5$  and mono  $\text{Co}_3\text{O}_4/\text{SmMn}_2\text{O}_5$ . (Test conditions: 0.2%  $\text{C}_3\text{H}_8$ , 2%  $\text{O}_2$ , 5%  $\text{H}_2\text{O}$  and balance gas  $\text{N}_2$  with a WHSV of 30,000  $\text{mL}\cdot\text{g}^{-1}\cdot\text{h}^{-1}$ ).

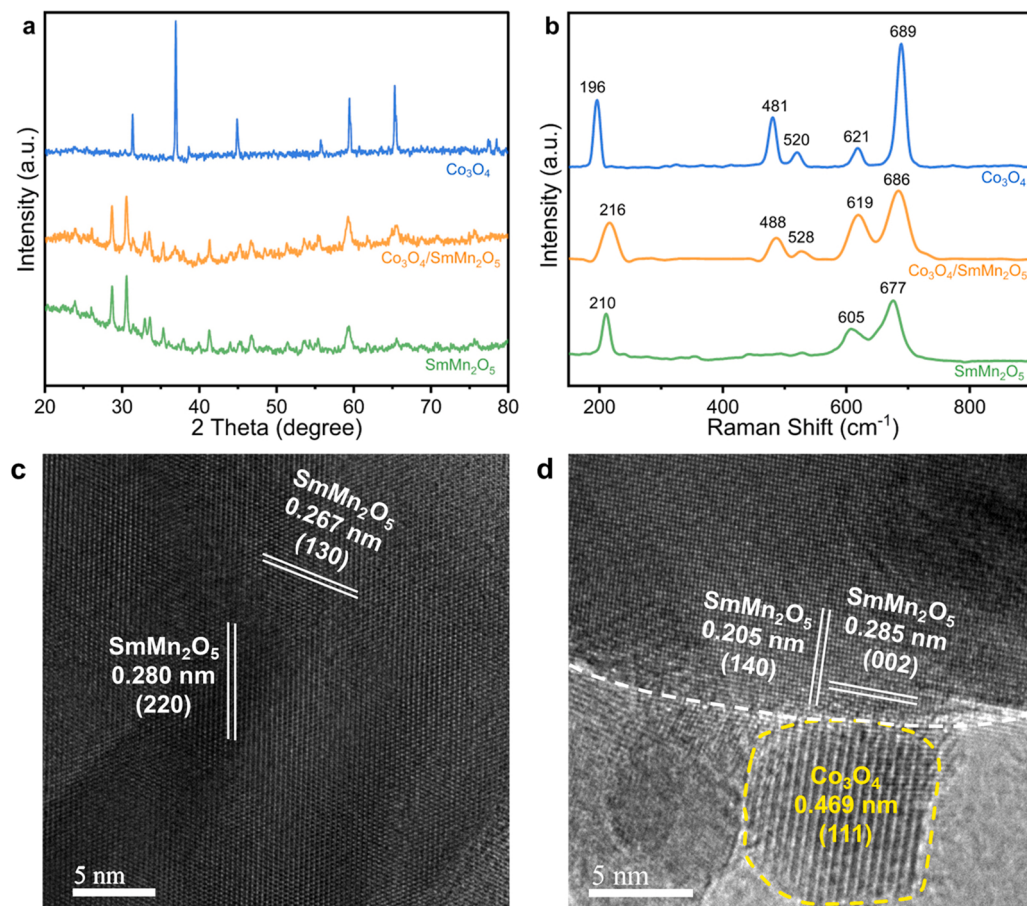


Fig. 2. (a) Powder XRD patterns; (b) Raman spectra of as-prepared catalysts; high-resolution TEM images of (c) SmMn<sub>2</sub>O<sub>5</sub> and (d) Co<sub>3</sub>O<sub>4</sub>/SmMn<sub>2</sub>O<sub>5</sub>.

50Co<sub>3</sub>O<sub>4</sub>/SmMn<sub>2</sub>O<sub>5</sub> possessed a maximum specific surface area and minimum pore size close to that of Co<sub>3</sub>O<sub>4</sub>, but did not exhibit the best catalytic performance, which may be attributed to the large mutual

accumulation of Co<sub>3</sub>O<sub>4</sub> over SmMn<sub>2</sub>O<sub>5</sub> rather than adequate contact with SmMn<sub>2</sub>O<sub>5</sub>. High-resolution TEM images for SmMn<sub>2</sub>O<sub>5</sub> and Co<sub>3</sub>O<sub>4</sub>/SmMn<sub>2</sub>O<sub>5</sub> were displayed in Figs. 2c, d and S9 with the

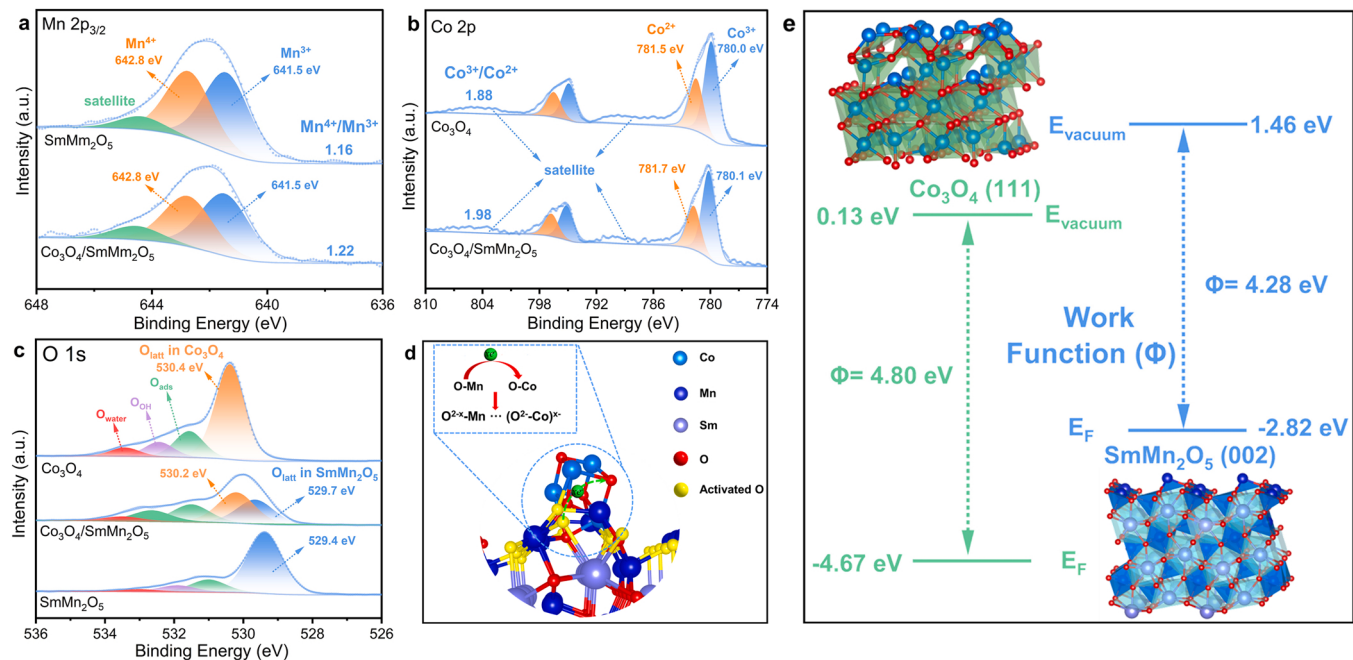


Fig. 3. (a-c) XPS spectra of Mn 2p<sub>3/2</sub>, Co 2p and O 1s; (d) activation mechanism of surface lattice oxygen in Co<sub>3</sub>O<sub>4</sub>/SmMn<sub>2</sub>O<sub>5</sub>; (e) work functions of Co<sub>3</sub>O<sub>4</sub> (111) and SmMn<sub>2</sub>O<sub>5</sub> (002), derived from DFT theoretical calculations.

corresponding interplanar spacings. The lattice fringes with spacing of 0.205, 0.267, 0.280, and 0.285 nm represented (140), (130), (220), and (002) crystal planes in  $\text{SmMn}_2\text{O}_5$ , respectively, while the interplanar spacing of 0.469 nm in  $\text{Co}_3\text{O}_4$  could be assigned to the (111) crystal plane. The obvious interfaces proved that the  $\text{Co}_3\text{O}_4$  nanoparticles were attached on the surface of  $\text{SmMn}_2\text{O}_5$ .

### 3.3. Chemical states of surface elements

To reveal the interactions between the  $\text{SmMn}_2\text{O}_5$  support and  $\text{Co}_3\text{O}_4$  nanoparticles, XPS tests have been conducted and the results were illustrated in Fig. 3. Mn 2p<sub>3/2</sub> XPS spectra displayed binding energies at 641.5 and 642.8 eV (Fig. 3a), attributed to the characteristic of  $\text{Mn}^{3+}$  and  $\text{Mn}^{4+}$  species over  $\text{SmMn}_2\text{O}_5$  [11,15]. For  $\text{Co}_3\text{O}_4/\text{SmMn}_2\text{O}_5$ , the binding energies of Mn and Sm species (Fig. S10) were basically unchanged after the introduction of  $\text{Co}_3\text{O}_4$ , but the ratio of  $\text{Mn}^{4+}/\text{Mn}^{3+}$  increased slightly from 1.16 to 1.22, resulting in more oxygen vacancies in the  $\text{Co}_3\text{O}_4/\text{SmMn}_2\text{O}_5$ , which provided more adsorption sites for oxygen molecules [26,27]. Fig. 3b presented the Co 2p XPS profiles of  $\text{Co}_3\text{O}_4$  and  $\text{Co}_3\text{O}_4/\text{SmMn}_2\text{O}_5$ . The Co 2p XPS profile of  $\text{Co}_3\text{O}_4$  can be deconvoluted into four components of  $\text{Co}^{3+}$  (780.0 eV),  $\text{Co}^{2+}$  (781.5 eV),  $\text{Co}^{3+}$  (795.0 eV),  $\text{Co}^{2+}$  (796.5 eV) [28]. The binding energies of  $\text{Co}^{3+}$  and  $\text{Co}^{2+}$  shifted to 780.1, 781.7, 795.1, and 796.7 eV over  $\text{Co}_3\text{O}_4/\text{SmMn}_2\text{O}_5$  respectively, indicating the presence of electron transfer from Co to O sites in  $\text{Co}_3\text{O}_4$  phase [18]. The above phenomenon was further confirmed by the O 1s XPS results. As depicted in Fig. 3c, O 1s spectrum of pure  $\text{SmMn}_2\text{O}_5$  was fitted into four components, including  $\text{O}_{\text{latt}}$  at 529.4 eV, surface adsorbed oxygen ( $\text{O}_{\text{ads}}$ ) at 531.0 eV, adsorbed hydroxyl ( $\text{O}_{\text{OH}}$ ) at 531.9 eV and adsorbed molecular water ( $\text{O}_{\text{water}}$ ) at 533.0 eV [29–31]. Similarly, O 1s spectrum of pure  $\text{Co}_3\text{O}_4$  was composed of  $\text{O}_{\text{latt}}$  at 530.4 eV,  $\text{O}_{\text{ads}}$  at 531.5 eV,  $\text{O}_{\text{OH}}$  at 532.4 eV and  $\text{O}_{\text{water}}$  at 533.4 eV. In contrast, for  $\text{Co}_3\text{O}_4/\text{SmMn}_2\text{O}_5$ , both peaks attributed to  $\text{O}_{\text{latt}}$  species in  $\text{Co}_3\text{O}_4$  and  $\text{SmMn}_2\text{O}_5$  phases were observed. Significantly, the binding energy of  $\text{O}_{\text{latt}}$  species in  $\text{Co}_3\text{O}_4$  phase became weaker compared to individual  $\text{Co}_3\text{O}_4$ , while that over  $\text{SmMn}_2\text{O}_5$  phase behaved the opposite change. These results indicated that electrons in the O sites of  $\text{SmMn}_2\text{O}_5$  were transferred into the O sites of  $\text{Co}_3\text{O}_4$  (Fig. 3d), causing the inactive lattice oxygen ( $\text{O}^{2-}$ ) over  $\text{SmMn}_2\text{O}_5$  being activated as  $\text{O}^{2-x}$  due to the strong interface interactions [18]. In addition, O 1s results demonstrated that the  $\text{O}_{\text{ads}}/(\text{O}_{\text{latt}}+\text{O}_{\text{ads}})$  ratio of  $\text{Co}_3\text{O}_4/\text{SmMn}_2\text{O}_5$  (31.4%) was higher than that of  $\text{SmMn}_2\text{O}_5$  (20.9%) (Table S3), suggesting that  $\text{Co}_3\text{O}_4/\text{SmMn}_2\text{O}_5$  displayed more surface oxygen species than  $\text{SmMn}_2\text{O}_5$ . Additionally, the full widths at half maxima (FWHM) of the fitted peaks for each species were shown in Table S4. The above results can be verified by the work functions of  $\text{Co}_3\text{O}_4$  (111) and  $\text{SmMn}_2\text{O}_5$  (002) (Fig. 3e). It is easier for the interface electrons to migrate from the phase with the lower WF to the phase with the higher WF, which is essential for understanding interface interactions [32]. As the work function of  $\text{SmMn}_2\text{O}_5$  (4.28 eV) was smaller than that of  $\text{Co}_3\text{O}_4$  (4.80 eV), the electrons of the former were more

prone to be excited and subsequently transferred to the latter during the composite catalyst preparation process, as corroborated by the XPS O1s results. As a result, the  $\text{O}_{\text{latt}}$  activation of  $\text{SmMn}_2\text{O}_5$  around the interface arose from the change of its charge density.

### 3.4. Characterization of active oxygen species

The reducibility of as-synthesized catalysts was evaluated by  $\text{H}_2$ -TPR, and the results were shown in Fig. 4a. The peaks centered at 275 and 440 °C were caused by the reduction of  $\text{Co}^{3+}$  to  $\text{Co}^{2+}$  and  $\text{Co}^{2+}$  to metallic Co in  $\text{Co}_3\text{O}_4/\text{SmMn}_2\text{O}_5$  [33,34]. The area ratio of the two peaks were 1: 3, consistent with the stoichiometric ratio of  $\text{Co}^{3+}$  to  $\text{Co}^{2+}$  in  $\text{Co}_3\text{O}_4$ , whose two reduction peaks appeared at 281 and 415 °C. Meanwhile, the peaks centered at 374 and 486 °C for  $\text{Co}_3\text{O}_4/\text{SmMn}_2\text{O}_5$  could be assigned to the reduction of  $\text{Mn}^{4+}$  to  $\text{Mn}^{3+}$  and  $\text{Mn}^{3+}$  to  $\text{Mn}^{2+}$ , respectively, lower than those of  $\text{SmMn}_2\text{O}_5$  (405 and 501 °C), demonstrating that the interface interaction between  $\text{Co}_3\text{O}_4$  and  $\text{SmMn}_2\text{O}_5$  improved the reducibility of Mn species and  $\text{Co}_3\text{O}_4/\text{SmMn}_2\text{O}_5$  was more reducible.

To evaluate the effect of in situ growth of  $\text{Co}_3\text{O}_4$  nanoparticles over  $\text{SmMn}_2\text{O}_5$  on the  $\text{O}_{\text{latt}}$  mobility,  $\text{O}_2$ -TPD experiments over as-synthesized catalysts were carried out. As shown in Fig. 4b, the desorption temperature of surface  $\text{O}_{\text{latt}}$  in  $\text{SmMn}_2\text{O}_5$  phase over  $\text{Co}_3\text{O}_4/\text{SmMn}_2\text{O}_5$  (356 °C) was evidently lower than that of  $\text{SmMn}_2\text{O}_5$  (405 °C), in accordance with the  $\text{H}_2$ -TPR results, implying that  $\text{O}_{\text{latt}}$  species in  $\text{SmMn}_2\text{O}_5$  in the vicinity of the interface were easier to be released and react with the substrate. The above results demonstrated the interface construction between  $\text{Co}_3\text{O}_4$  and  $\text{SmMn}_2\text{O}_5$  induced the effective activation of  $\text{O}_{\text{latt}}$ . Furthermore, pure  $\text{SmMn}_2\text{O}_5$  and  $\text{Co}_3\text{O}_4$  were mechanically mixed to obtain  $\text{Co}_3\text{O}_4+\text{SmMn}_2\text{O}_5$  mixture according to the actual ratio of  $\text{Co}_3\text{O}_4$  and  $\text{SmMn}_2\text{O}_5$  in  $\text{Co}_3\text{O}_4/\text{SmMn}_2\text{O}_5$  (Table S3). It was clearly shown that  $\text{Co}_3\text{O}_4/\text{SmMn}_2\text{O}_5$  displayed much higher catalytic activity than  $\text{Co}_3\text{O}_4+\text{SmMn}_2\text{O}_5$  mixture under the same reaction conditions (Fig. S11), benefiting from the  $\text{O}_{\text{latt}}$  activation due to the existence of interface.

Based on the above results, it was evident that the activation of interfacial  $\text{O}_{\text{latt}}$  was crucial to achieve high activity of  $\text{Co}_3\text{O}_4/\text{SmMn}_2\text{O}_5$ . Considering that the content and dispersion of  $\text{Co}_3\text{O}_4$  were bound to dominate in the activation of interfacial  $\text{O}_{\text{latt}}$ , the dispersion of  $\text{Co}_3\text{O}_4$  in  $x\text{Co}_3\text{O}_4/\text{SmMn}_2\text{O}_5$  with different loadings was probed through  $\text{H}_2$  pulse chemisorption experiments (Fig. S12). With the increase of  $\text{Co}_3\text{O}_4$  content, more  $\text{Co}_3\text{O}_4/\text{SmMn}_2\text{O}_5$  interface was formed, conducive to activating more interfacial  $\text{O}_{\text{latt}}$  (Fig. 1e and Table S5). Nevertheless, the further increase led to the larger particle, resulting in a decrease in  $\text{Co}_3\text{O}_4$  dispersion and no participation in the activation of interfacial  $\text{O}_{\text{latt}}$ . Accordingly, there was an optimal content of 30% for maximum activation of interfacial  $\text{O}_{\text{latt}}$ .

To evaluate the changes in the water resistance of  $\text{SmMn}_2\text{O}_5$  before and after the introduction of  $\text{Co}_3\text{O}_4$  particles,  $\text{H}_2\text{O}$ -TPD experiments were conducted. Fig. 4c showed the profiles of the normalized mass

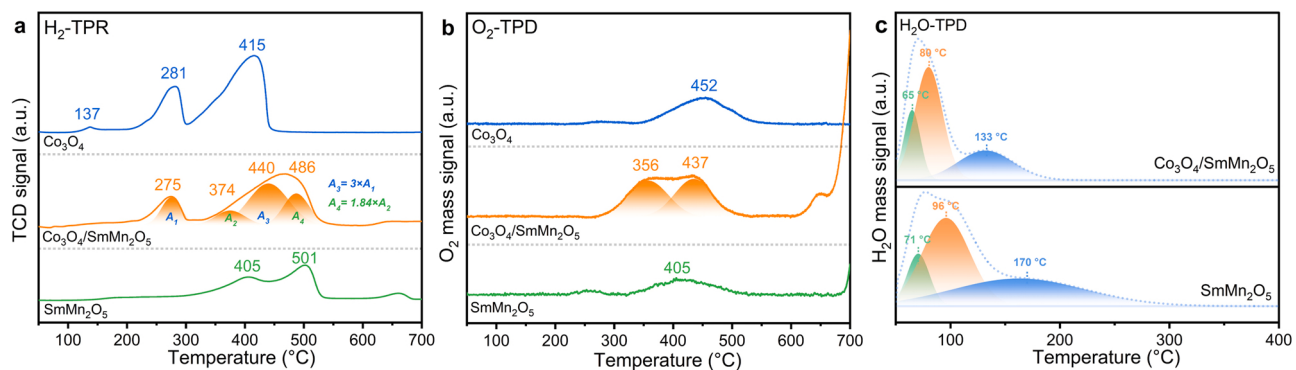


Fig. 4. (a)  $\text{H}_2$ -TPR and (b)  $\text{O}_2$ -TPD profiles of  $\text{Co}_3\text{O}_4$ ,  $\text{SmMn}_2\text{O}_5$  and  $\text{Co}_3\text{O}_4/\text{SmMn}_2\text{O}_5$ ; (c)  $\text{H}_2\text{O}$ -TPD profiles of  $\text{SmMn}_2\text{O}_5$  and  $\text{Co}_3\text{O}_4/\text{SmMn}_2\text{O}_5$ .

response of  $\text{H}_2\text{O}$  versus the temperature of  $\text{SmMn}_2\text{O}_5$  and  $\text{Co}_3\text{O}_4/\text{SmMn}_2\text{O}_5$ . It was observed that the presence of  $\text{Co}_3\text{O}_4$  particles makes it more difficult to adsorb water on the  $\text{SmMn}_2\text{O}_5$  surface, whether it was physically adsorbed ( $< 120^\circ\text{C}$ ) or hydrogen bonded ( $120\text{--}200^\circ\text{C}$ ) [35], and thus  $\text{Co}_3\text{O}_4/\text{SmMn}_2\text{O}_5$  could exhibit excellent hydrothermal stability.

The roles of gaseous oxygen and lattice oxygen in propane combustion reaction were studied by  $\text{C}_3\text{H}_8$ -TPSR. As shown in Fig. 5a, with the introduction of gaseous oxygen, the temperature at which  $\text{CO}_2$  started to be generated of  $\text{Co}_3\text{O}_4/\text{SmMn}_2\text{O}_5$  ( $168^\circ\text{C}$ ) was lower than that of  $\text{SmMn}_2\text{O}_5$  ( $207^\circ\text{C}$ ), mainly benefitting from the more active chemisorbed oxygen ( $\text{O}_2^-$  and  $\text{O}^-$ ) over  $\text{Co}_3\text{O}_4/\text{SmMn}_2\text{O}_5$ . Meanwhile, the  $\text{Co}_3\text{O}_4/\text{SmMn}_2\text{O}_5$  was endowed with more active  $\text{O}_{\text{latt}}$  by interface interaction, enabling the complete conversion of propane at  $282^\circ\text{C}$ , which was achieved on  $\text{SmMn}_2\text{O}_5$  over  $370^\circ\text{C}$ . It is also important to note that the water desorption temperature of  $\text{Co}_3\text{O}_4/\text{SmMn}_2\text{O}_5$  decreased to  $240^\circ\text{C}$  compared with that of unmodified  $\text{SmMn}_2\text{O}_5$  ( $276^\circ\text{C}$ ), indicating that the former exhibit a better hydrophobicity with great resistance to water, which made propane more dominant in competitive adsorption. In the absence of gaseous oxygen, chemisorbed oxygen was rapidly consumed, followed by  $\text{O}_{\text{latt}}$  dominating the propane combustion, as reflected in Fig. 5b. It is worth noting that the temperature at which  $\text{O}_{\text{latt}}$  functioned was  $352^\circ\text{C}$  on  $\text{SmMn}_2\text{O}_5$ , substantially higher than  $307^\circ\text{C}$  on  $\text{Co}_3\text{O}_4/\text{SmMn}_2\text{O}_5$ , which echoed the  $\text{O}_2$ -TPD results. To demonstrate the enhanced effect of Co introduction on propane adsorption, the  $\text{C}_3\text{H}_8$ -TPD experiments were conducted, as illustrated in Fig. 5c. A distinct propane desorption peak at  $95^\circ\text{C}$  was observed on  $\text{SmMn}_2\text{O}_5$ , while only a smoother desorption peak was observed at  $182^\circ\text{C}$  on  $\text{Co}_3\text{O}_4/\text{SmMn}_2\text{O}_5$ , pointing to a stronger propane adsorption capacity of the latter.

### 3.5. Density functional theory (DFT) calculations

The  $\text{O}_{\text{latt}}$  activation via the interface interactions between  $\text{Co}_3\text{O}_4$  and  $\text{SmMn}_2\text{O}_5$  was further verified by DFT computations. The unit cell of  $\text{SmMn}_2\text{O}_5$ , the optimized geometries of  $\text{SmMn}_2\text{O}_5$  and  $\text{Co}_3\text{O}_4/\text{SmMn}_2\text{O}_5$  were shown in Figs. S13–S15. The propane adsorption energies and the formation energy of oxygen vacancies at various sites including over

$\text{SmMn}_2\text{O}_5$  phase,  $\text{Co}_3\text{O}_4$  phase, and  $\text{SmMn}_2\text{O}_5$  in the vicinity of  $\text{Co}_3\text{O}_4$  were compared. The propane gas adsorption energy ( $E_{\text{ads}}$ ) was acquired via the following equation (Eq. (1)).

$$E_{\text{ads}} = E_{\text{after adsorption}} - E_{\text{before adsorption}} - E_{\text{propane}} \quad (1)$$

where  $E_{\text{after adsorption}}$ ,  $E_{\text{before adsorption}}$ ,  $E_{\text{propane}}$  represent the total energy of the optimized propane gas adsorbed on the  $\text{Co}_3\text{O}_4/\text{SmMn}_2\text{O}_5$  surface, the energy of the  $\text{Co}_3\text{O}_4/\text{SmMn}_2\text{O}_5$  surface, and the energy of a propane gas molecule, respectively [20]. Ordinarily, the more negative the value of  $E_{\text{ads}}$ , the stronger the adsorption ability. The optimized propane adsorption models over three different sites were shown in Fig. 6a. The corresponding  $E_{\text{ads}}$  values (Table 1) of propane followed the order:  $\text{SmMn}_2\text{O}_5$  in the vicinity of  $\text{Co}_3\text{O}_4$  ( $|-0.22\text{ eV}|$ )  $>$   $\text{SmMn}_2\text{O}_5$  phase ( $|-0.13\text{ eV}|$ )  $>$   $\text{Co}_3\text{O}_4$  phase ( $|-0.09\text{ eV}|$ ). These results indicated that propane preferred to adsorb over  $\text{SmMn}_2\text{O}_5$  in the vicinity of  $\text{Co}_3\text{O}_4$  rather than the  $\text{SmMn}_2\text{O}_5$  phase or  $\text{Co}_3\text{O}_4$  phase, suggesting that O sites over  $\text{SmMn}_2\text{O}_5$  in the vicinity of  $\text{Co}_3\text{O}_4$  were the main sites where the propane oxidation reaction proceeded, owing to the electrophilic nature formed by the charge reduction.

Based on the  $\text{O}_2$ -TPD and  $\text{H}_2$ -TPR results, the activity enhancement induced by the  $\text{Co}_3\text{O}_4$  introduction was most likely ascribed to the activation of  $\text{O}_{\text{latt}}$ . In order to confirm the effect of in situ growth of  $\text{Co}_3\text{O}_4$  over  $\text{SmMn}_2\text{O}_5$  on  $\text{O}_{\text{latt}}$  activity, the oxygen vacancy formation energies of  $\text{SmMn}_2\text{O}_5$  and  $\text{Co}_3\text{O}_4/\text{SmMn}_2\text{O}_5$  were calculated. The oxygen vacancy formation energy ( $E_{\text{f}}(V_0)$ ) was obtained according to the following equation (Eq. (2)).

$$E_{\text{f}}(V_0) = E(V_0) - E(\text{ideal}) + 1/2 E(\text{O}_2) \quad (2)$$

where  $E(V_0)$ ,  $E(\text{ideal})$ , and  $E(\text{O}_2)$  are the total energies of the defect-containing supercell, ideal supercell, and an  $\text{O}_2$  molecule, respectively [36]. In the ideal crystal structure of  $\text{SmMn}_2\text{O}_5$  (Fig. 6b), each oxygen atom is coordinated with two or three manganese atoms. After introducing a unit of  $\text{Co}_3\text{O}_4$ , all the Mn–O distances in the vicinity of  $\text{Co}_3\text{O}_4$  were elongated, as compiled in Table 1. Accordingly, the  $E_{\text{f}}(V_0)$  of  $\text{SmMn}_2\text{O}_5$  in the vicinity of  $\text{Co}_3\text{O}_4$  decreased dramatically relative to those of  $\text{SmMn}_2\text{O}_5$ . In particular, the  $\text{O}_2$  via additionally coordinating to a Co atom showed the largest change in  $E_{\text{f}}(V_0)$  from  $2.15\text{ eV}$  in  $\text{SmMn}_2\text{O}_5$

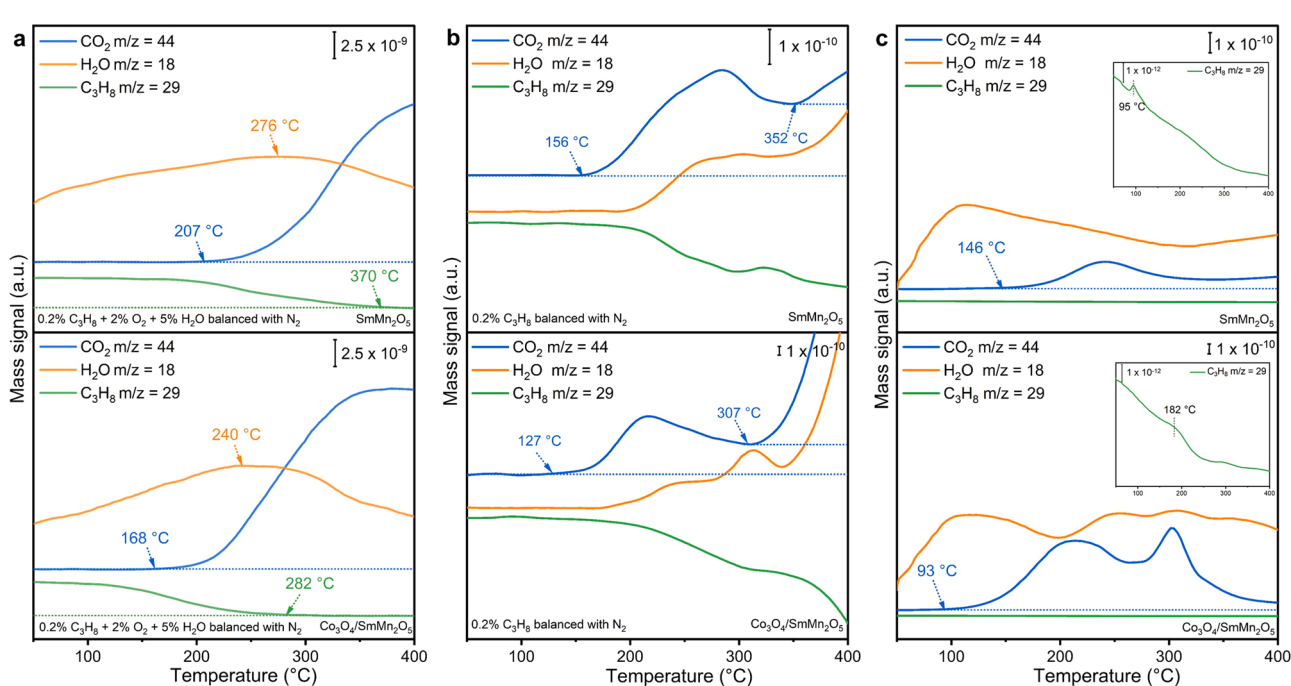


**Fig. 5.** TPSR profiles of propane (a) with  $\text{O}_2$  and (b) without  $\text{O}_2$ ; (c) TPD profiles of propane on  $\text{SmMn}_2\text{O}_5$  and  $\text{Co}_3\text{O}_4/\text{SmMn}_2\text{O}_5$ . (Test conditions of TPSR: 0.2%  $\text{C}_3\text{H}_8$ , with or without 2%  $\text{O}_2$  and 5%  $\text{H}_2\text{O}$ , and balance gas  $\text{N}_2$  with a WHSV of  $30,000\text{ mL}^{-1}\text{h}^{-1}$ ).

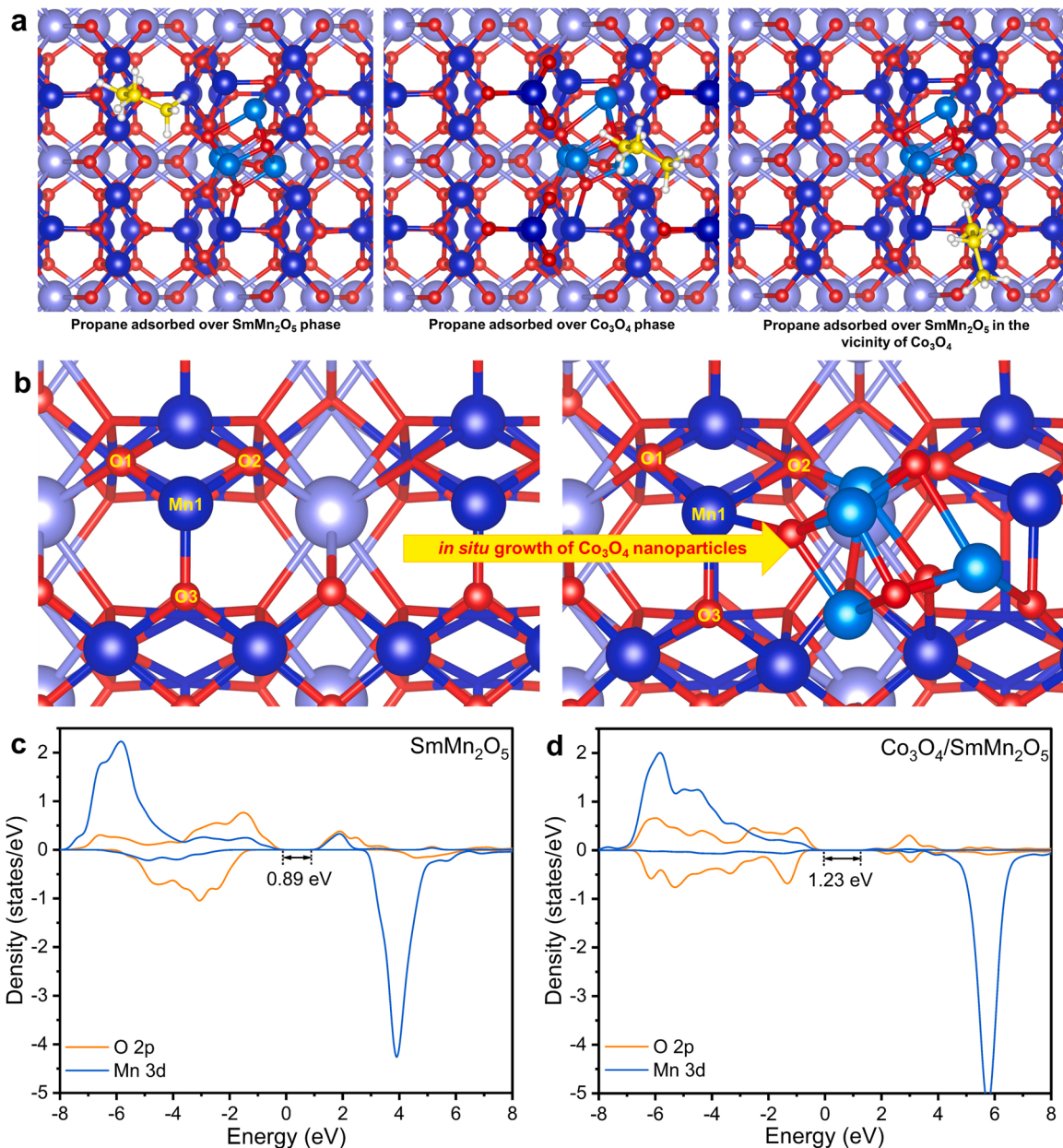


**Fig. 6.** (a) DFT calculation models for propane adsorbed over SmMn<sub>2</sub>O<sub>5</sub> phase, Co<sub>3</sub>O<sub>4</sub> phase and SmMn<sub>2</sub>O<sub>5</sub> in the vicinity of Co<sub>3</sub>O<sub>4</sub>, respectively; (b) structure optimization of SmMn<sub>2</sub>O<sub>5</sub> and Co<sub>3</sub>O<sub>4</sub>/SmMn<sub>2</sub>O<sub>5</sub>; PDOS of (c) SmMn<sub>2</sub>O<sub>5</sub> and (d) Co<sub>3</sub>O<sub>4</sub>/SmMn<sub>2</sub>O<sub>5</sub>. (The blue, red, lavender, cyan, yellow, and white represent manganese, oxygen, samarium, cobalt, carbon, and hydrogen, respectively; The atoms discussed in the PDOS are Mn1 and O2 in Fig. 4b.)

**Table 1**

The propane gas adsorption energies, the formation energies of oxygen vacancy and Mn-O bond lengths.

Adsorption sites	$E_{\text{ads}}$ /eV	Mn-O/Å	$E_f(V_0)$ /eV
SmMn <sub>2</sub> O <sub>5</sub> phase	-0.09	O1	2.023, 1.788
		O2	2.033, 1.790
		O3	1.851, 1.987, 1.987
Co <sub>3</sub> O <sub>4</sub> phase	-0.13	–	
Co <sub>3</sub> O <sub>4</sub> /SmMn <sub>2</sub> O <sub>5</sub>	-0.22	O1	2.089, 1.938
		O2	2.482, 2.213
		O3	2.005, 2.050, 2.078
			2.86

to 1.72 eV in Co<sub>3</sub>O<sub>4</sub>/SmMn<sub>2</sub>O<sub>5</sub>. The  $E_f(V_0)$  for O3 also decreased to 2.86 eV in Co<sub>3</sub>O<sub>4</sub>/SmMn<sub>2</sub>O<sub>5</sub> by 0.38 eV. The considerable reduction of the  $E_f(V_0)$  of SmMn<sub>2</sub>O<sub>5</sub> after introducing Co<sub>3</sub>O<sub>4</sub> makes Co<sub>3</sub>O<sub>4</sub>/SmMn<sub>2</sub>O<sub>5</sub> the best ability to form surface oxygen vacancy and the most abundant

active oxygen species over the surface, which are most crucial for propane combustion.

To further investigate the interactions between the orbitals, the PDOS of different catalysts were analyzed (Fig. 6c, d). In contrast to the interaction between Mn-O atomic orbitals in pure SmMn<sub>2</sub>O<sub>5</sub>, the introduction of Co<sub>3</sub>O<sub>4</sub> led to a more localized atomic orbital of Mn and a decrease in the mutual overlap between Mn and O atomic orbitals, implying a weakened bond between Mn-O. Meanwhile, PDOS also indicate that the introduction of Co<sub>3</sub>O<sub>4</sub> broadened the forbidden band width (from 0.89 to 1.23 eV), demonstrating that the electron transfer from the 2p orbitals of O atoms to the empty 3d orbitals of Mn atoms was further suppressed, which likewise predicted the weakening of the Mn-O bond.

### 3.6. Analysis of intermediate species in propane oxidation

*In situ* DRIFTS was conducted to explore the dynamic nature of  $\text{SmMn}_2\text{O}_5$  and  $\text{Co}_3\text{O}_4/\text{SmMn}_2\text{O}_5$  catalysts for propane combustion. As shown in Fig. 7a, b, when the chamber was purged with feed gas consisting of 0.2% propane and balance gas nitrogen at 25 °C, absorption bands at 2800–3000 cm<sup>-1</sup> were detectable for  $\text{SmMn}_2\text{O}_5$  and  $\text{Co}_3\text{O}_4/\text{SmMn}_2\text{O}_5$ , assigned to the absorption of gaseous propane [37]. Moreover, multiple bands corresponding to carboxylate and carbonate species were observed at 1000–1700 cm<sup>-1</sup> [38]. The peaks of monodentate carbonate (1275 and 1530 cm<sup>-1</sup>), polydentate carbonate (1340 cm<sup>-1</sup>), propionate (1470 cm<sup>-1</sup>), acetate (1550 cm<sup>-1</sup>) and formate (1587 cm<sup>-1</sup>) appeared together [36,37,39–41], indicating the participation of  $\text{O}_{\text{latt}}$  of  $\text{SmMn}_2\text{O}_5$  and  $\text{Co}_3\text{O}_4/\text{SmMn}_2\text{O}_5$  in the propane oxidation. In order to understand the role of oxygen in the propane combustion reaction, *in situ* DRIFTS were performed with feed consisting of 0.2% propane, 2% oxygen, 5% water and balance gas nitrogen from 25 to 300 °C. All spectra in Fig. 7c, d were collected within 30 min of the oxidation reaction at the specific temperature. For  $\text{SmMn}_2\text{O}_5$  (Fig. 7c), the strong water signals (1640 and 3300–3500 cm<sup>-1</sup>) were still present at 150 °C, implying high occupation of active sites by water. In contrast, for  $\text{Co}_3\text{O}_4/\text{SmMn}_2\text{O}_5$  (Fig. 7d), the water signals at 100 °C were significantly reduced, attributing to the enhanced hydrophobicity due to  $\text{Co}_3\text{O}_4$  loading [42], which in turn allowed  $\text{Co}_3\text{O}_4/\text{SmMn}_2\text{O}_5$  to possess more superior water resistance. Besides, with the introduction of oxygen, the peaks attributed to acetone (1430 and 1674 cm<sup>-1</sup>) and propionaldehyde (1720 cm<sup>-1</sup>) then largely disappeared and the peaks

assigned to alkoxide species (1066 and 1165 cm<sup>-1</sup>) were significantly weakened [43–47], probably due to the deep oxidation of these intermediates accelerated by oxygen. It was of interest to pinpoint that the peak intensities of most intermediates over  $\text{Co}_3\text{O}_4/\text{SmMn}_2\text{O}_5$  were significantly weaker than those of  $\text{SmMn}_2\text{O}_5$  under anaerobic conditions, whereas the peak intensities of most carbonates over the former were obviously stronger than those of the latter under aerobic conditions. This may be responsible for the existence of more active  $\text{O}_{\text{latt}}$  in  $\text{Co}_3\text{O}_4/\text{SmMn}_2\text{O}_5$ , which allowed more intermediates to be deeply oxidized. Following the introduction of oxygen, the depleted  $\text{O}_{\text{latt}}$  was replenished and more substrates were further oxidized to carbonates.

Combined with the above experimental and theoretical results, the possible reaction paths of propane combustion over  $\text{Co}_3\text{O}_4/\text{SmMn}_2\text{O}_5$  were speculated and shown in Fig. 8. Propane was firstly oxidized to propionic acid (corresponding to the peak at 1470 cm<sup>-1</sup>), acetone (1430 and 1674) and propionaldehyde (1720 cm<sup>-1</sup>), verified by the  $\text{C}_3\text{H}_8$ -TPSR results (Fig. S16). Subsequently, the C-C bonds of both were broken and further oxidized to acetic acid (1550 cm<sup>-1</sup>), formic acid (1587 cm<sup>-1</sup>), and carbonic acid (1026, 1115, 1210, 1275, 1340, 1520 and 1530 cm<sup>-1</sup>), which were completely degraded to  $\text{CO}_2$  and  $\text{H}_2\text{O}$  finally. Due to the enhanced  $\text{O}_{\text{latt}}$  activity of  $\text{Co}_3\text{O}_4/\text{SmMn}_2\text{O}_5$  compared with  $\text{SmMn}_2\text{O}_5$ , the transformation of the intermediates was accelerated, leading to the much-improved propane combustion performance.

### 4. Conclusions

In this work, mullite  $\text{SmMn}_2\text{O}_5$  was employed for catalytic propane

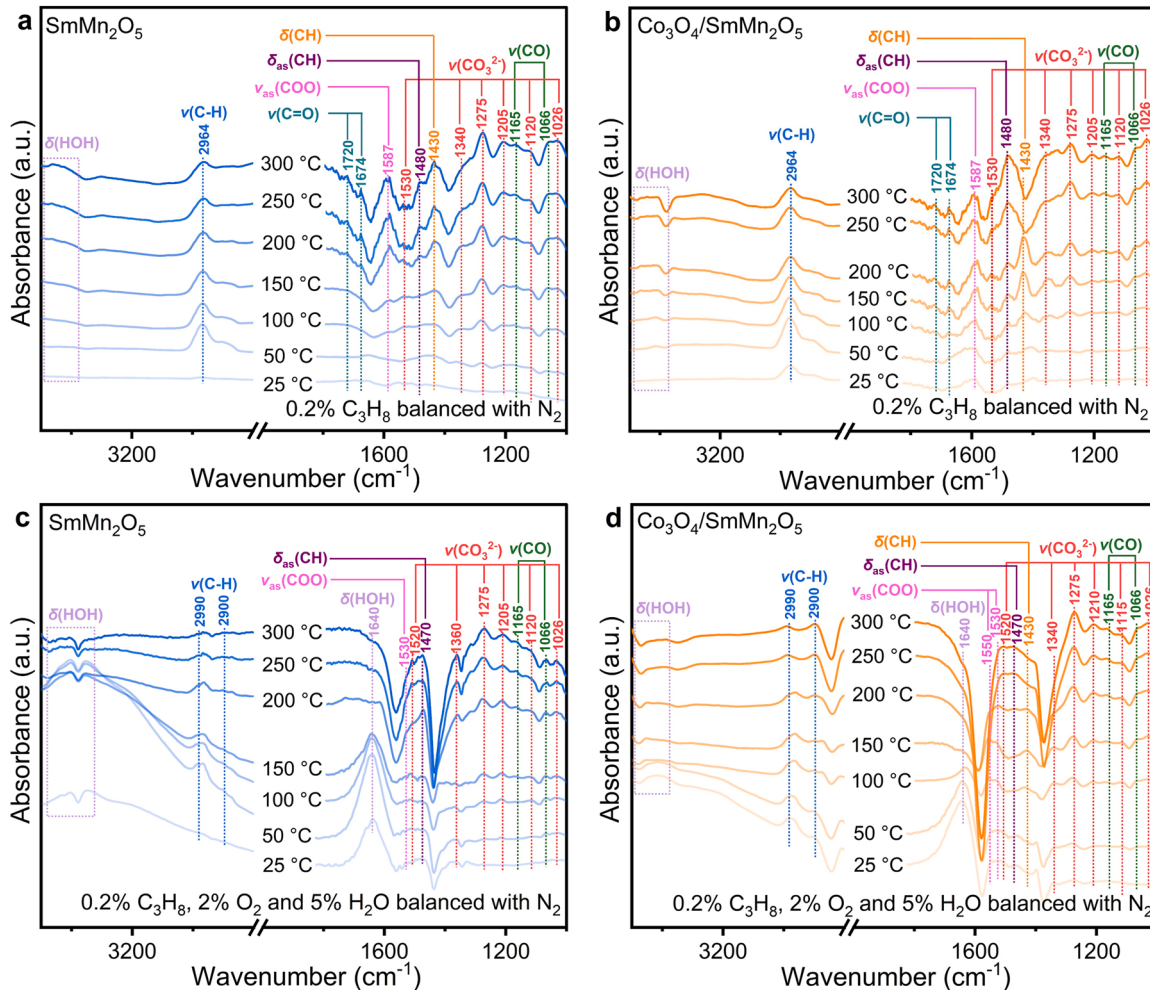


Fig. 7. DRIFT spectra of propane adsorption on (a)  $\text{SmMn}_2\text{O}_5$  and (b)  $\text{Co}_3\text{O}_4/\text{SmMn}_2\text{O}_5$ ; propane reaction with oxygen on (c)  $\text{SmMn}_2\text{O}_5$  and (d)  $\text{Co}_3\text{O}_4/\text{SmMn}_2\text{O}_5$ .

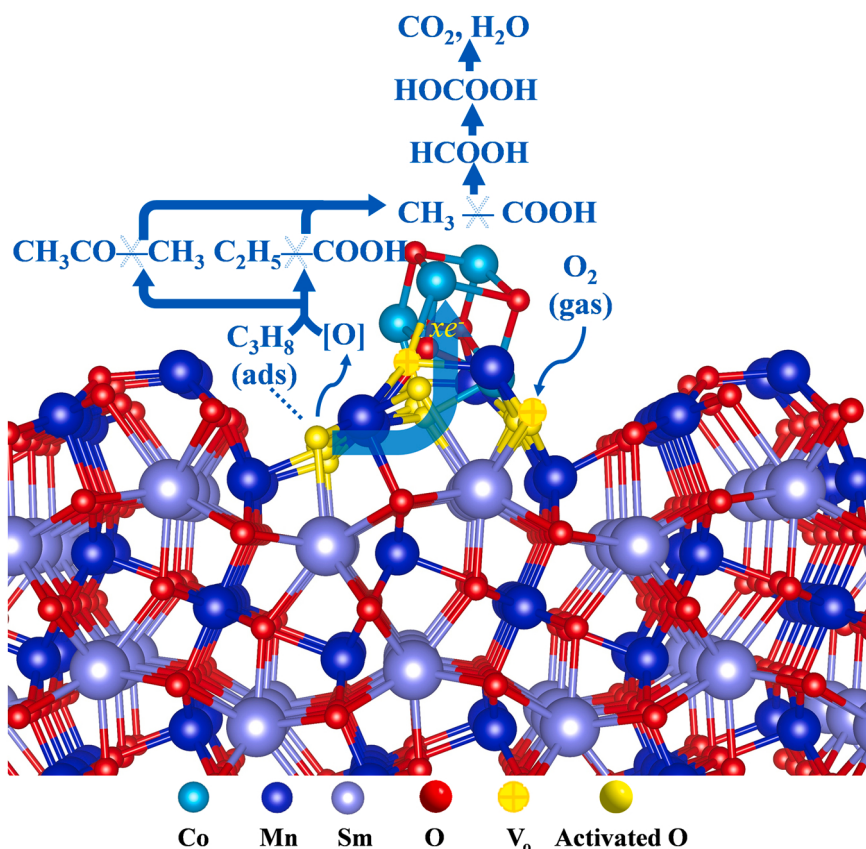


Fig. 8. Proposed  $\text{C}_3\text{H}_8$  oxidation reaction pathway over  $\text{Co}_3\text{O}_4/\text{SmMn}_2\text{O}_5$ .

combustion through interfacial engineering with  $\text{Co}_3\text{O}_4$ . The optimized  $\text{Co}_3\text{O}_4/\text{SmMn}_2\text{O}_5$  exhibited higher catalytic rate (39.6 vs. 14.4  $\mu\text{mol}_{\text{propane}} \cdot \text{m}_{\text{cat}}^{-2} \cdot \text{h}^{-1}$ ) and TOF (0.329 vs. 0.094  $\text{h}^{-1}$ ) than original  $\text{SmMn}_2\text{O}_5$ , as well as excellent high-temperature stability and reuse performance. HR-TEM images and XPS characterization proved that the formation of interface between  $\text{Co}_3\text{O}_4$  and  $\text{SmMn}_2\text{O}_5$  led to the electron transfer from O sites of  $\text{SmMn}_2\text{O}_5$  to O sites of  $\text{Co}_3\text{O}_4$ .  $\text{O}_2$ -TPD,  $\text{H}_2$ -TPR,  $\text{C}_3\text{H}_8$ -TPSR,  $\text{C}_3\text{H}_8$ -TPD and DFT theoretical calculation results demonstrated that the electron transfer resulted in the significant activation of the Mn-O bonds in the interface and the inactive lattice  $\text{O}^{2-}$  was transformed into electrophilic active lattice  $\text{O}^{2-x}$ , which was easier to adsorb and oxidize propane. This work emphasizes the pivotal role of  $\text{O}_{\text{latt}}$  in propane catalytic combustion reaction and develops a facile and universal method for  $\text{O}_{\text{latt}}$  activation.

#### CRediT authorship contribution statement

All persons who have made substantial contributions to the work reported in the manuscript approved the final version. **Yi Liu**: Conceptualization, Methodology, Investigation, Writing – original draft. **Haolu Hu**: Validation, Methodology, Investigation. **Jiamin Zheng**: Visualization. **Fei Xie**: Validation. **Huayu Gu**: Visualization. **Sadegh Rostamnia**: Writing – review & editing. **Fangfang Pan**: Writing – review & editing. **Xiao Liu**: Writing, Supervision, Funding acquisition – review & editing. **Lizhi Zhang**: Supervision.

#### Declaration of Competing Interest

The authors declare that they have no known competing financial interests or personal relationships that could have appeared to influence the work reported in this paper.

#### Data availability

Data will be made available on request.

#### Acknowledgments

We acknowledge the National Key Research and Development Program of China (2019YFC1806203), the National Natural Science Foundation of China (U21A20289, 21976066) for financial support.

#### Appendix A. Supplementary material

Supplementary data associated with this article can be found in the online version at [doi:10.1016/j.apcatb.2023.122649](https://doi.org/10.1016/j.apcatb.2023.122649).

#### References

- [1] Y.R. Liu, X. Li, W.M. Liao, A.P. Jia, Y.J. Wang, M.F. Luo, J.Q. Lu, Highly active Pt/BN catalysts for propane combustion: the roles of support and reactant-induced evolution of active sites, *ACS Catal.* 9 (2019) 1472–1481.
- [2] M.N. Taylor, W. Zhou, T. Garcia, B. Solsona, A.F. Carley, C.J. Kiely, S.H. Taylor, Synergy between tungsten and palladium supported on titania for the catalytic total oxidation of propane, *J. Catal.* 285 (2012) 103–114.
- [3] B. Solsona, E. Aylón, R. Murillo, A. Mastral, A.M. Monzonis, S. Agouram, T. E. Davies, S.H. Taylor, T. Garcia, Deep oxidation of pollutants using gold deposited on a high surface area cobalt oxide prepared by a nanocasting route, *J. Hazard. Mater.* 187 (2011) 544–552.
- [4] Z. Wang, Z. Huang, J.T. Brosnanhan, S. Zhang, Y. Guo, Y. Guo, L. Wang, Y. Wang, W. Zhan, Ru/CeO<sub>2</sub> catalyst with optimized CeO<sub>2</sub> support morphology and surface facets for propane combustion, *Environ. Sci. Technol.* 53 (2019) 5349–5358.
- [5] Y.L. Guo, M.C. Wen, G.Y. Li, T.C. An, Recent advances in VOC elimination by catalytic oxidation technology onto various nanoparticles catalysts: a critical review, *Appl. Catal. B Environ.* 281 (2021), 119447.
- [6] G. Salek, P. Alphonse, P. Dufour, S. Guillemet-Fritsch, C. Tenaillieu, Low-temperature carbon monoxide and propane total oxidation by nanocrystalline cobalt oxides, *Appl. Catal. B Environ.* 147 (2014) 1–7.

[7] J.A. Enterkin, W. Setthapun, J.W. Elam, S.T. Christensen, F.A. Rabuffetti, L. D. Marks, P.C. Stair, K.R. Poepelmeier, C.L. Marshall, Propane oxidation over Pt/SrTiO<sub>3</sub> nanocuboids, *ACS Catal.* 1 (2011) 629–635.

[8] Z. Hu, X. Liu, D. Meng, Y. Guo, Y. Guo, G. Lu, Effect of ceria crystal plane on the physicochemical and catalytic properties of Pd/ceria for CO and propane oxidation, *ACS Catal.* 6 (2016) 2265–2279.

[9] Y. Yao, Q. Su, X. Feng, B. Sun, W. Ji, C. Au, Active yet extremely durable Co<sub>3</sub>O<sub>4</sub> spheroids of different texture without/with Au deposition for CO oxidation, *Catal. Sci. Technol.* 5 (2015) 1065–1075.

[10] P. Zhao, P. Yu, Z. Feng, R. Chen, L. Jia, J. Wang, M. Shen, B. Shan, A mullite oxide catalyst of SmMn<sub>2</sub>O<sub>5</sub> for three-way catalysis: synthesis, characterization, and catalytic activity evaluation, *RSC Adv.* 6 (2016) 65950–65959.

[11] B.F. Jin, B.H. Zhao, S. Liu, Z.G. Li, K.X. Li, R. Ran, Z.C. Si, D. Weng, X.D. Wu, SmMn<sub>2</sub>O<sub>5</sub> catalysts modified with silver for soot oxidation: dispersion of silver and distortion of mullite, *Appl. Catal. B Environ.* 273 (2020), 119058.

[12] Y.P. Zheng, S. Thampy, N. Ashburn, S. Dillon, L.H. Wang, Y. Jiangou, K. Tan, F. T. Kong, Y.F. Nie, M.J. Kim, W.S. Epling, Y.J. Chabal, J.W.P. Hsu, K. Cho, Stable and active oxidation catalysis by cooperative lattice oxygen redox on SmMn<sub>2</sub>O<sub>5</sub> mullite surface, *J. Am. Chem. Soc.* 141 (2019) 10722–10728.

[13] J. Yang, J. Zhang, X. Liu, X. Duan, Y. Wen, R. Chen, B. Shan, Origin of the superior activity of surface doped SmMn<sub>2</sub>O<sub>5</sub> mullites for NO oxidation: a first-principles based microkinetic study, *J. Catal.* 359 (2018) 122–129.

[14] R. Liu, B. Zhou, L. Liu, Y. Zhang, Y. Chen, Q. Zhang, M. Yang, L. Hu, M. Wang, Y. Tang, Enhanced catalytic oxidation of VOCs over porous Mn-based mullite synthesized by in-situ dismutation, *J. Colloid Interface Sci.* 585 (2021) 302–311.

[15] X. Wan, L. Wang, S. Gao, X. Lang, L. Wang, T. Zhang, A. Dong, W. Wang, Low-temperature removal of aromatics pollutants via surface labile oxygen over Mn-based mullite catalyst SmMn<sub>2</sub>O<sub>5</sub>, *Chem. Eng. J.* 410 (2021), 128305.

[16] T. Zhang, X. Lang, A. Dong, X. Wan, S. Gao, L. Wang, L. Wang, W. Wang, Difference of oxidation mechanism between light C3-C4 alkane and alkene over mullite YMn<sub>2</sub>O<sub>5</sub> oxides catalyst, *ACS Catal.* 10 (2020) 7269–7282.

[17] Y.R. Fang, L. Li, J. Yang, S. Hoang, L.M. Wang, J. Xu, W.W. Yang, C.Q. Pan, Y. H. Zhu, H.T. Deng, Z. Luo, C.Z. Sun, D.Q. Gao, Z.G. Li, Y.B. Guo, Engineering the nucleophilic active oxygen species in CuTiO<sub>4</sub> for efficient low-temperature propene combustion, *Environ. Sci. Technol.* 54 (2020) 15476–15488.

[18] X. Wang, Z. Pan, X. Chu, K. Huang, Y. Cong, R. Cao, R. Sarangi, L. Li, G. Li, S. Feng, Atomic-scale insights into surface lattice oxygen activation at the spinel/perovskite interface of Co<sub>3</sub>O<sub>4</sub>/La<sub>0.3</sub>Sr<sub>0.7</sub>CoO<sub>3</sub>, *Angew. Chem. Int. Ed.* 131 (2019) 11846–11851.

[19] L. Wang, Z.H. Hu, X. Wan, W.X. Hua, H. Li, Q.-H. Yang, W.C. Wang, Li<sub>2</sub>S<sub>4</sub> anchoring governs the catalytic sulfur reduction on defective SmMn<sub>2</sub>O<sub>5</sub> in lithium-sulfur battery, *Adv. Energy Mater.* 20 (2022) 2200340.

[20] X.Y. Chen, B.J. Sun, J.Y. Chu, Z. Han, Y. Wang, Y.C. Du, X.J. Han, P. Xu, Oxygen vacancy-induced construction of CoO/h-TiO<sub>2</sub> Z-scheme heterostructures for enhanced photocatalytic hydrogen evolution, *ACS Appl. Mater. Interfaces* 25 (2022) 28945–28955.

[21] W. Liu, W.J. Xiang, N.N. Guan, R.Y. Cui, H. Cheng, X. Chen, Z.X. Song, X.J. Zhang, Y.M. Zhang, Enhanced catalytic performance for toluene purification over Co<sub>3</sub>O<sub>4</sub>/MnO<sub>2</sub> catalyst through the construction of different Co<sub>3</sub>O<sub>4</sub>-MnO<sub>2</sub> interface, *Sep. Purif. Technol.* 278 (2022), 119590.

[22] Q. Yu, C. Liu, X. Li, C. Wang, X. Wang, H. Cao, M. Zhao, G. Wu, W. Su, T. Ma, J. Zhang, H. Bao, J. Wang, B. Ding, M. He, Y. Yamauchi, X.S. Zhao, N-doping activated defective Co<sub>3</sub>O<sub>4</sub> as an efficient catalyst for low-temperature methane oxidation, *Appl. Catal. B Environ.* 269 (2020), 118757.

[23] Y.J. Shen, J. Deng, L.P. Han, W. Ren, D.S. Zhang, Low-temperature combustion of toluene over Cu-doped SmMn<sub>2</sub>O<sub>5</sub> mullite catalysts via creating highly active Cu<sup>2+</sup>-O-Mn<sup>4+</sup> sites, *Environ. Sci. Technol.* 56 (2022) 10433–10441.

[24] W. Tang, W. Xiao, S. Wang, Z. Ren, J. Ding, P.-X. Gao, Boosting catalytic propane oxidation over PGM-free Co<sub>3</sub>O<sub>4</sub> nanocrystal aggregates through chemical leaching: a comparative study with Pt and Pd based catalysts, *Appl. Catal. B Environ.* 226 (2018) 585–595.

[25] Y.N. Zhu, C. Du, Z.J. Feng, Y.J. Chen, H. Li, R. Chen, M.Q. Shen, B. Shan, Highly dispersed Pd on macroporous SmMn<sub>2</sub>O<sub>5</sub> mullite for low temperature oxidation of CO and C<sub>3</sub>H<sub>8</sub>, *RSC Adv.* 8 (2018) 5459–5467.

[26] Q.L. Yang, X. Wang, X.Y. Wang, Q. Li, L. Li, W.N. Yang, X.F. Chu, H. Liu, J.S. Men, Y. Peng, Y.L. Ma, J.H. Li, Surface reconstruction of a mullite-type catalyst via selective dissolution for NO oxidation, *ACS Catal.* 11 (2021) 14507–14520.

[27] Z.-Y. Tian, P.H.T. Ngamou, V. Vannier, K. Kohse-Höinghaus, N. Bahlawane, Catalytic oxidation of VOCs over mixed Co-Mn oxides, *Appl. Catal. B Environ.* 17 (2012) 1125–1134.

[28] M.C. Zhang, X. Sui, X. Zhang, M. Niu, C.Q. Li, H.Q. Wan, Z.-A. Qiao, H.J. Xie, X. Y. Li, Multi-defects engineering of NiCo<sub>2</sub>O<sub>4</sub> for catalytic propane oxidation, *Appl. Surf. Sci.* 600 (2022), 154040.

[29] H. Najjar, J.-F. Lamonier, O. Mentré, J.-M. Giraudon, H. Batis, Optimization of the combustion synthesis towards efficient LaMn<sub>3+y</sub> catalysts in methane oxidation, *Appl. Catal. B Environ.* 106 (2011) 149–159.

[30] C. Zhang, Y. Guo, G. Lu, A. Boreave, L. Retailleau, A. Baylet, A. Giroir-Fendler, LaMn<sub>3</sub>O<sub>9</sub> perovskite oxides prepared by different methods for catalytic oxidation of toluene, *Appl. Catal. B Environ.* 148 (2014) 490–498.

[31] M. Sathiya, G. Rousse, K. Ramesha, C. Laisa, H. Vezin, M.T. Sougrati, M.-L. Doublet, D. Foix, D. Gonbeau, W. Walker, Reversible anionic redox chemistry in high-capacity layered-oxide electrodes, *Nat. Mater.* 12 (2013) 827–835.

[32] Y.S. Ma, X.L. Liu, M.Y. Tang, K.F. Du, H.Y. Yin, X.H. Mao, D.H. Wang, Waste eggshell-derived N, P, S tri-doped core-shell catalysts for efficient Fenton-like catalysis, *Chem. Eng. J.* 440 (2022), 135879.

[33] L.R. Bao, S.H. Zhu, Y. Chen, Y. Wang, W.H. Meng, S. Xu, Z.H. Lin, X.Y. Li, M. Sun, L.M. Guo, Anionic defects engineering of Co<sub>3</sub>O<sub>4</sub> catalyst for toluene oxidation, *Fuel* 314 (2022), 122774.

[34] L. Ma, C.Y. Seo, X.Y. Chen, K. Sun, J.W. Schwank, Indium-doped Co<sub>3</sub>O<sub>4</sub> nanorods for catalytic oxidation of CO and C<sub>3</sub>H<sub>6</sub> towards diesel exhaust, *Appl. Catal. B Environ.* 222 (2018) 44–58.

[35] X.D. Zhang, F.K. Bi, Z.Q. Zhu, Y. Yang, S.H. Zhao, J.F. Chen, X.T. Lv, Y.X. Wang, J. C. Xu, N. Liu, The promoting effect of H<sub>2</sub>O on rod-like MnCeO<sub>x</sub> derived from MOFs for toluene oxidation: a combined experimental and theoretical investigation, *Appl. Catal. B Environ.* 297 (2021), 120393.

[36] Z. Ren, Z. Wu, W. Song, W. Xiao, Y. Guo, J. Ding, S.L. Suib, P.X. Gao, Low temperature propane oxidation over Co<sub>3</sub>O<sub>4</sub> based nano-array catalysts: Ni dopant effect, reaction mechanism and structural stability, *Appl. Catal. B Environ.* 180 (2016) 150–160.

[37] Z. Hu, Z. Wang, Y. Guo, L. Wang, Y. Guo, J. Zhang, W. Zhan, Total oxidation of propane over a Ru/CeO<sub>2</sub> catalyst at low temperature, *Environ. Sci. Technol.* 52 (2018) 9531–9541.

[38] W. Zhu, X. Chen, Z. Liu, C. Liang, Insight into the effect of cobalt substitution on the catalytic performance of LaMn<sub>3</sub>O<sub>9</sub> perovskites for total oxidation of propane, *J. Phys. Chem. C* 124 (2020) 14646–14657.

[39] Z. Hu, S. Qiu, Y. You, Y. Guo, Y.L. Guo, L. Wang, W.C. Zhan, G.Z. Lu, Hydrothermal synthesis of NiCeO<sub>x</sub> nanosheets and its application to the total oxidation of propane, *Appl. Catal. B Environ.* 225 (2018) 110–120.

[40] L. Ma, Y. Geng, X.Y. Chen, N.Q. Yan, J.H. Li, J.W. Schwankb, Reaction mechanism of propane oxidation over Co<sub>3</sub>O<sub>4</sub> nanorods as rivals of platinum catalysts, *Chem. Eng. J.* 402 (2020), 125911.

[41] W. Zhu, X. Chen, J. Jin, X. Di, C. Liang, Z. Liu, Insight into catalytic properties of Co<sub>3</sub>O<sub>4</sub>-CeO<sub>2</sub> binary oxides for propane total oxidation, *Chin. J. Catal.* 41 (2020) 679–690.

[42] C.L. Ni, J.T. Hou, Q. Zheng, M.Q. Wang, L. Ren, M.X. Wang, W.F. Tan, Insights into a “seesaw effect” between reducibility and hydrophobicity induced by cobalt doping: influence on OMS-2 nanomaterials for catalytic degradation of carcinogenic benzene, *Environ. Sci. Nano* 8 (2021) 3376–3386.

[43] L. Chen, Y. Zhu, H. Zheng, C. Zhang, Y. Li, Aqueous-phase hydrodeoxygenation of propanoic acid over the Ru/ZrO<sub>2</sub> and Ru-Mo/ZrO<sub>2</sub> catalysts, *Appl. Catal. A Gen.* 411 (2012) 95–104.

[44] S. Gerei, E. Rozhkovka, Y.B. Gorokhovatsky, Propylene and oxygen chemisorption on cupric oxide and cuprous oxide catalysts, *J. Catal.* 28 (1973) 341–350.

[45] K.-H. Dostert, C.P. O'Brien, F. Mirabella, F. Ivars-Barceló, S. Schauerermann, Adsorption of acrolein, propanal, and allyl alcohol on Pd(111): a combined infrared reflection-absorption spectroscopy and temperature programmed desorption study, *Phys. Chem. Chem. Phys.* 18 (2016) 13960–13973.

[46] H. Kareem, Y. Maswadeh, Z.P. Wu, A.C. Leff, H.W. Cheng, S.Y. Shan, S. Wang, R. Robinson, D. Caracciolo, A. Langrock, D.M. Mackie, D.T. Tran, V. Petkov, C. J. Zhong, Lattice strain and surface activity of ternary nanoalloys under the propane oxidation condition, *ACS Appl. Mater. Interfaces* 9 (2022) 11435–11447.

[47] X.Y. Ma, Y.T. Tang, Y.F. Liu, Y. Zhang, L.W. Jia, X. Liu, C. Du, B. Shan, A-site cation exfoliation of amorphous SmMn<sub>x</sub>O<sub>y</sub> oxides for low temperature propane oxidation, *J. Catal.* 409 (2022) 59–69.